Experimental Study of Spectrally Selective MEMS/Metasurface Infrared Detectors

Melisa Ekin Gülseren, *Member, IEEE*, Matthew Benson, Ryan W. Parker, Jeronimo Segovia-Fernandez, *Member, IEEE*, Ernest Ting-Ta Yen, *Member, IEEE*, and J. Sebastián Gómez-Díaz, *Senior Member, IEEE*

***Abstract*—This article reports a comprehensive statistical analysis of uncooled infrared (IR) detectors based on radio frequency (RF) aluminum nitride (AlN) contour mode resonators (CMRs) integrated with spectrally selective IR metasurfaces. Moreover, it reports the lowest noise equivalent power (NEP) recorded from these types of devices (~11 pW/$\sqrt{\text{Hz}}$). The metasurfaces are printed on top of the AlN resonator body to decouple mechanical, RF, and IR responses. Optical lithography is used to pattern the metasurfaces, allowing the fabrication of hundreds of spectrally selective IR detectors with different sensing performances within the same chip. An automated characterization system is employed to quickly record parameters such as quality factor, noise, and responsivity. This approach allows to experimentally determine the geometrical dimensions of quasi-optimal IR detectors that exhibit NEP in the pW/$\sqrt{\text{Hz}}$ range and responsivities in the Hz/nW range. Additionally, the detector performance versus IR light is explored using different interrogation mechanisms, namely monitoring the CMR resonance frequency as well as the amplitude and phase of an RF signal that excites the device at resonance. The statistical analysis of hundreds of IR sensors reveals trends between parameters such quality factor and noise floor, and NEP and responsivity. These trends provide useful guidelines for the development of quasi-optimal spectrally selective IR sensors operating at room temperature.**

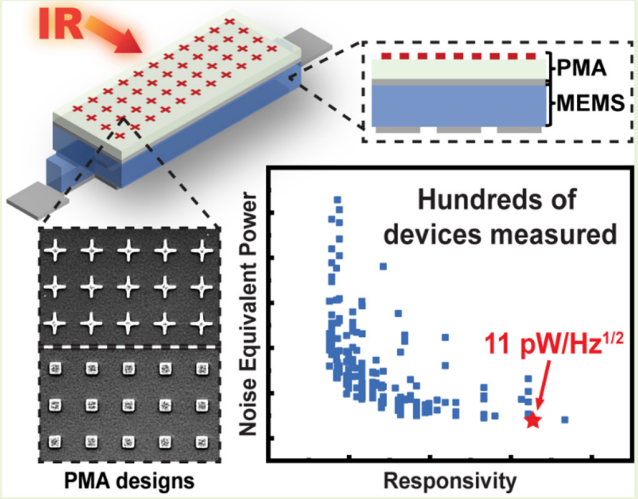

***Index Terms*—Aluminum nitride (AlN), infrared (IR) detector, microelectromechanical system (MEMS) resonator, metasurface, perfect material absorber.**

I. Introduction

INFRARED (IR) detectors have originally been of interest for military applications such as night vision, missile tracking, target recognition, and surveillance [1]. Thanks to recent advances in IR detectors operating at room temperature, IR technologies have expanded into civilian products, with a wide field of application in areas such as medical diagnosis, biological and chemical threat detection, electrical power system inspection, and IR spectroscopy [2]. These developments have been fueled by the emergence of new technologies enabling the production of highly sensitive and low-cost uncooled detectors [3]. Recent research in IR detectors has been focused on improving sensitivity, reducing noise, increasing speed, and reducing cost. Researchers are exploring new materials such as graphene, perovskites, and quantum dots for use in IR detectors based on photodetection [4], [5], [6]. Even though these materials may offer advantages such as higher sensitivity and lower cost, they usually exhibit better performance when operated at low temperatures [7]. One significant technology for IR detection has been based on microelectromechanical system (MEMS) devices, in which thin films of materials that absorb IR radiation are combined with MEMS to convert the IR into an easily detectable electrical signal.

Manuscript received 17 January 2024; revised 9 April 2024; accepted 9 April 2024. Date of publication 19 April 2024; date of current version 31 May 2024. This work was supported in part by the Department of Defense–Army under Grant W911NF2210067, in part by the Semiconductor Research Corporation under Project 1806387/Task 2810.050, in part by the National Institutes of Health under Award R01CA273253, and in part by the National Science Foundation under Award ECCS 2314932. The associate editor coordinating the review of this article and approving it for publication was Prof. Pai-Yen Chen. *(Corresponding author: J. Sebastián Gómez-Díaz.)*

Melisa Ekin Gülseren, Matthew Benson, Ryan W. Parker, and J. Sebastián Gómez-Díaz are with the Electrical and Computer Engineering Department, University of California, Davis, CA 95616 USA (e-mail: mgulseren@ucdavis.edu; mrbenson@ucdavis.edu; rwparker@ucdavis.edu; jsgomez@ucdavis.edu).

Jeronimo Segovia-Fernandez and Ernest Ting-Ta Yen are with Kilby Labs–Texas Instrument, Santa Clara, CA 95051 USA (e-mail: jeronimo.segovia@ti.com; ernest.ttyen@ti.com).

Digital Object Identifier 10.1109/JSEN.2024.3388966

Such IR detectors based on gallium nitride [8] and quartz [9] have been demonstrated in the past with some promise, while more exotic configurations relying on barium strontium titanate [10], black phosphorous [11], or graphene [12] based resonant MEMS detectors have also been reported in recent years. On top of being reliant on production techniques that are not compatible with conventional CMOS processes and integrated circuits, approaches based on incorporating a lossy material into the resonant structure of a MEMS are only typically capable of achieving a limited amount of IR absorption, translating into low detection capability, power efficiency, and noise equivalent power (NEP).

In addition to these material-based approaches, researchers have also explored novel detector designs and architectures. For example, some researchers have developed IR detectors that use metamaterials [13], [14] which are engineered structures that exhibit tailored electromagnetic properties. These detectors offer enhanced sensitivity and selectivity, as well as the ability to detect specific wavelengths of IR radiation. The working principle is based on combining a perfect metasurface absorber (PMA) with a MEMS possessing a negative temperature-frequency coefficient (TCF). A PMA is an engineered structure, consisting of a periodic array of subwavelength structures, that interacts with incident light to produce a resonance and absorb incoming radiation [15]. The absorption of IR radiation leads to an increase in the temperature of the MEMS device, which results in a decrease in the resonance frequency due to the negative TCF. Thus, the incident IR radiation can be detected from the resonance frequency shift of the MEMS device [16]. The complete first demonstration of this concept, by Hui et al. [17], incorporated a thin piezoelectric plasmonic metasurface composed of nanoplates into the resonant body of a contour mode resonator (CMR), and reported a moderately low NEP $\sim$2.1 nW/$\sqrt{\text{Hz}}$ at the target wavelength of 8.8 μm, for which $\sim$80% spectral absorption was achieved. In a further work, Hui et al. [18] demonstrated a similar design incorporating a fishnet-based metasurface for MWIR detection, reporting an NEP of $\sim$1.9 nW/$\sqrt{\text{Hz}}$ for $\sim$60% spectral absorption. Tao et al. [19] reported the co-integration of a PMA with a film bulk acoustic wave resonator (FBAR), allowing the achievement of both high absorptivity and high sensitivity, demonstrating absorption of 88% at around 8.2 μm and an NEP $\sim$ 0.2 nW/$\sqrt{\text{Hz}}$. An analogous technology was proposed by Tan et al. [20], in which a PMA is integrated with a pyroelectric detector. Multiple pyroelectric elements with different detection wavelengths (i.e., different PMA designs) were demonstrated for the detection of eight different gases, achieving NEP of 19 nW/$\sqrt{\text{Hz}}$ with >60% spectral absorption in the $\sim$2–8 μm range, for the eight reported designs [20].

Perhaps the most crucial parameter in evaluating the performance of an IR sensor is the NEP, which is defined as the IR power that gives a signal-to-noise ratio equal to 1 in a 1 Hz measurement bandwidth and represents the minimum detectable IR power. It is typically measured as the ratio between the frequency spectral noise density, extracted from measurements of the short-term frequency stability, and the responsivity, extracted from the frequency response under IR illumination, usually a blackbody radiator. As such, these measurements are typically carried out by wire-bonding individual detectors to packaging, making it cumbersome and tedious to characterize and study a large number of detectors. Additionally, the fabrication of PMAs integrated with MEMS has relied so far upon electron beam lithography, a slow and expensive process that hinders the fabrication of multiple IR detectors within the same chip. Taken together, these factors explain why most works have only reported one or very few IR detectors based on MEMS/PMAs. Furthermore, due to the challenges of fabricating and characterizing many devices, the optimization of the PMA and the MEMS designs have usually been performed separately, i.e., designing the metasurface PMA unit cell to maximize absorption in the target IR range, and designing the MEMS geometry to maximize thermal resistance, which would ideally result in an optimal IR detector. However, this approach neglects potential cross-coupling effects between the PMA and the MEMS, and it has not been yet experimentally demonstrated.

In this work, we present a performance analysis of hundreds of IR detectors with varying MEMS and PMA designs, aiming to provide useful guidelines for the design of quasi-optimal IR detectors. We fabricate and characterize a co-integrated aluminum nitride (AlN)-based CMR with a PMA incorporated on top in a CMOS-compatible process [21]. DUV optical lithography is utilized instead of electron beam lithography for the PMA fabrication, enabling the easy fabrication of a larger number of varying designs. Multiple spectrally selective IR metasurface designs are fabricated on identical MEMS structures, allowing the exploration of their influence in the sensing metrics. Additionally, an automated on-wafer RF/IR measurement system has been developed to enable the characterization of hundreds of devices, quickly obtaining metrics such as quality factor, fluctuation-induced noise, NEP, and responsivity. This allows us to perform a comprehensive statistical analysis on the performance of IR sensors, revealing the trends among various metrics of interest and reporting quasi-optimal devices with NEP in the pW/$\sqrt{\text{Hz}}$ range. We experimentally demonstrate that NEP and responsivity, as well as the quality factor and the fluctuation-induced noise, are related inversely. Our study helps simplify and streamline the design procedure for quasi-optimal MEMS-based resonant IR sensors, which can open new opportunities for their application in many fields.

II. Device Design and Fabrication

The IR detector consists of a co-integrated CMR and PMA, as shown in Fig. 1. The CMR is composed of an AlN film sandwiched between two Pt electrodes [22]. The common configuration for a CMR is a single electrode connected to the ground for the bottom electrode, and an interdigitated top electrode with electrode widths of W. Upon applying an ac signal, a contour-extensional mode of vibration, with a center frequency of $f_0 = (1/2W)(E_{\text{eq}}/\rho_{\text{eq}})^{1/2}$, given an equivalent Young's modulus of E_{eq} and equivalent mass density ρ_{eq}, is excited in the AlN film through its equivalent d_{31} piezoelectric coefficient [23]. The devices reverse the ground and interdigitated electrode [see Fig. 1(b)], which allows the ground electrode to be used simultaneously as a continuous

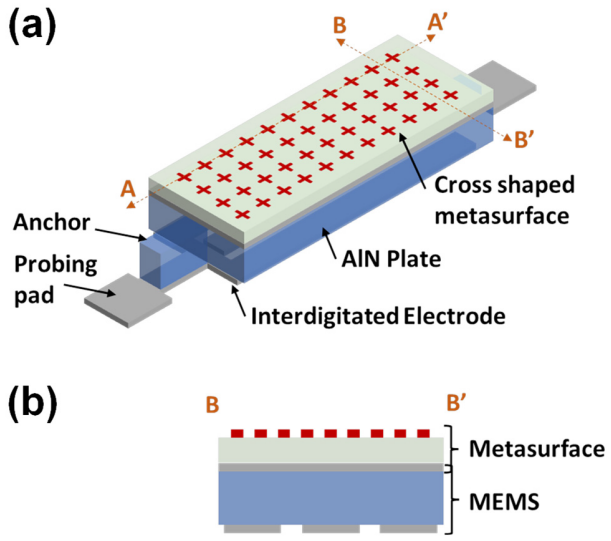

Fig. 1. (a) Three-dimensional schematic of the co-integrated lateral CMR MEMS and perfect metamaterial absorber IR detector. (b) Cross-sectional schematic of the device showing the common plane for the resonator top electrode and metasurface ground plane.

plane for the ground layer of the PMA. The PMA provides additional mechanical loading for the CMR; however, has little effect on the overall performance of the device due to its ultrathin (∼200 nm) nature. A three-electrode resonator with a total active area of 60 × 125 μm^2 and an AlN thickness of 1 μm was used as the resonator "base." This resonator "base" was designed for a fundamental resonance at 208 MHz, and we followed the studies of anchor losses in [24] and [25] to methodically vary Q by changing the anchor dimensions, and thus systematically study the effect of Q on device performance. The goal is to experimentally assess how the mechanical quality factor of the MEMS affects the sensing performance of the devices in terms of NEP, responsivity, and noise. The anchor width (W_a) ranged from 5 to 30 μm, with a step size of 5 μm, and the anchor length (L_a) ranged from 12 to 62 μm, with a step size of 10 μm. Thus, there are a total of 36 resonator designs composed of identical MEMS bodies but anchors with different geometries. A total of 20 repetitions of each resonator design were fabricated, and each one was loaded with a different metasurface design. These metasurfaces are composed of unit cells with different geometries and dimensions (see Table I) and target absorption peaks at ∼4 and ∼5.5 μm. Therefore, a total of 720 IR sensors are fabricated and characterized in this study.

A metal-insulator-metal IR absorber composes the PMA. The top electrode of the CMR is combined with a SiO_2 film and patterned Al nanostructures. SiO_2 was chosen for the dielectric layer for its smaller TCF relative to AlN, in order to make the TCF of the IR detector device mainly dependent on the AlN. The thickness of the SiO_2 layer was set to 200 nm and the period of the PMA unit cell ranged around 4 μm. Aluminum nanostructures, see scanning electron microscope (SEM) images in the lower-left insets of Fig. 2(a), were used for the top layer to provide good spectral sensitivity as well as good polarization and angle independence with respect to the incoming waves [26], [27], [28]. Selectivity is defined here

TABLE I
SUMMARY OF THE MEASURED IR ABSORPTION PROFILES ASSOCIATED WITH THE DETECTORS SHOWN IN FIG. 2. EACH ROW CORRESPONDS TO A DIFFERENT METASURFACE DESIGN, COMPOSED OF NANORESONATORS WITH DIFFERENT WIDTH (a), LENGTH (b), AND PERIODICITY (P). RESULTS INCLUDE THE TARGETED WAVELENGTH (λ_{PEAK}), MAXIMUM ABSORPTION (A_{PEAK}), AND FWHM

#	Width, a (μm)	Length, b (μm)	Period, P (μm)	λ_{peak} (μm)	A_{peak} (%)	FWHM (nm)
1*	1.11	1.11	3.5	3.78	79	465
2*	1.14	1.14	3.5	3.86	81	466
3*	1.17	1.17	3.5	3.96	82	502
4	0.25	1.34	3.2	3.22	71	408
5	0.45	1.34	3.2	3.62	83	474
6	0.65	1.34	3.2	3.92	81	544
7	0.35	1.31	3.5	3.51	76	472
8	0.35	1.34	3.5	3.50	73	421
9	0.35	1.37	3.5	3.56	75	424
10	1.87	1.87	4.5	5.93	91	528
11	1.90	1.90	4.5	6.04	94	500
12	1.93	1.93	4.5	6.09	91	510
13*	0.35	2.17	3.5	5.35	95	450
14*	0.35	2.20	3.5	5.40	94	448
15*	0.35	2.23	3.5	5.50	94	466
16	0.45	2.17	3.9	4.50	79	523
17	0.45	2.20	3.9	5.53	91	440
18	0.45	2.23	3.9	5.61	92	475
19	0.45	2.18	3.2	5.39	98	533
20	0.65	2.18	3.2	5.64	98	619

* Denotes the devices shown in Fig. 4.

in terms of the full-width half maximum (FWHM) of the absorption profile. The choice of unit-cell nanostructure that composes the metasurface is the determining factor in terms of IR absorption, i.e., peak absorption wavelength and FWHM, in addition to polarization sensitivity [26], and in this study, we explored both cross and patch-shaped nanostructures. The unit cell of the nanostructures was defined by a, the cross width, b, the cross length, and P, the period of the repeating unit cell; for patch-shaped nanostructures $a = b$. For both the cross and patch-shaped nanostructures, designs optimizing absorption at wavelengths of ∼4 and ∼5.5 μm were made, and then the geometric dimensions producing the optimized design were slightly altered to introduce variation (see Table I). Upon incidence of IR light, the PMA structure absorbs the targeted IR wavelengths within its geometry, converting electromagnetic energy into thermal energy. The thermal energy heats the CMR up and down-shifts its resonance frequency.

The devices were fabricated using a combination of deep UV (DUV) photolithography, depositions, and etching, as summarized in Fig. 3. A high-resistivity Si wafer was used as the substrate. A 10 nm chromium and 100 nm platinum were sputter deposited (Lesker Labline Sputter) to form the bottom electrodes using a lift-off process. The piezoelectric body of the resonators was formed by ac sputtering (Endeavor AT) 1 μm of AlN. Vias to the bottom electrode were etched using a TCP system in a Cl_2 environment. A Cr/Pt (10/100 nm) metal layer serving the double purpose of top electrode for the resonators and ground plane for the metasurfaces was sputter deposited and patterned using lift-off.

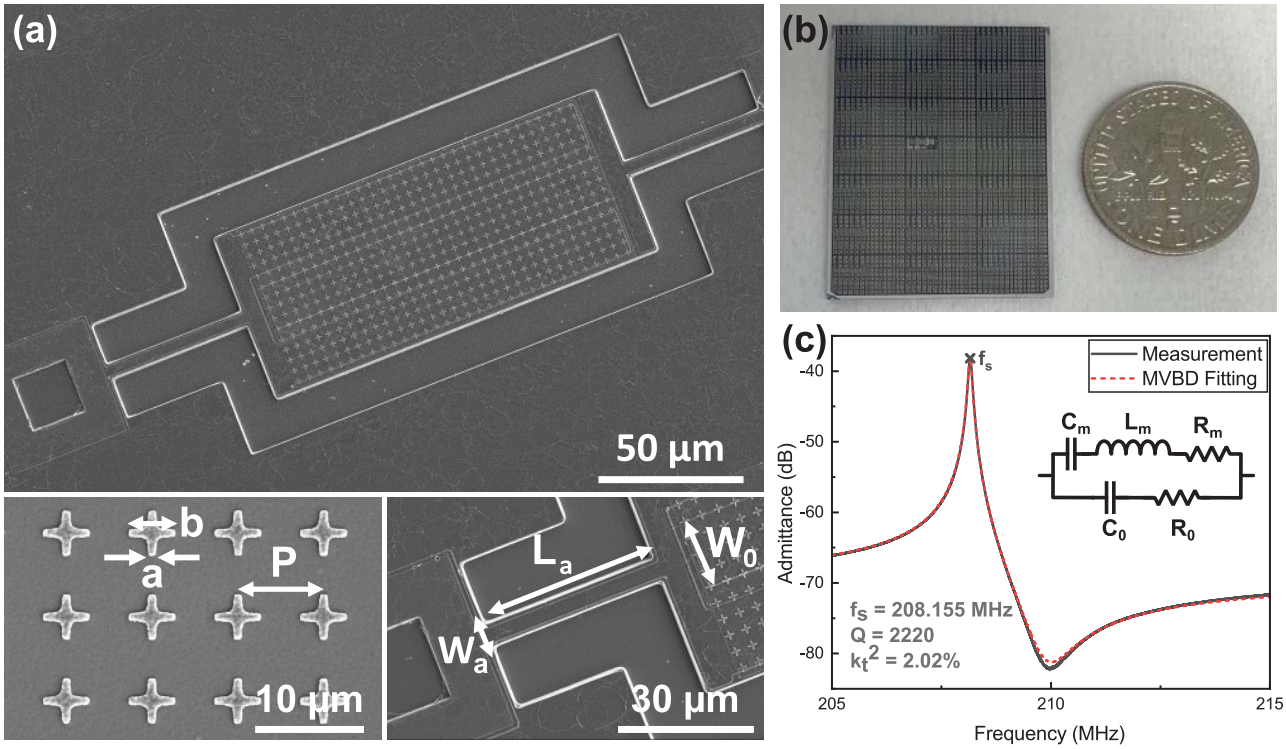

Fig. 2. (a) SEM images showing an IR sensor (top) and details of the metasurface (bottom-left) and MEMS anchors (bottom right). (b) Photograph of a 2.2 × 2.7 cm chip containing hundreds of different IR sensors. A US dime is also shown for scale. (c) Admittance parameters response (dB) of a high-Q MEMS device with $W_a = 15$ μm and $L_a = 12$ μm. MBVD fitting [33] shows good agreement, with circuit parameters extracted as $R_0 = 735$ Ω, $R_m = 81$ Ω, $C_0 = 260$ fF, $C_m = 4.25$ fF, $L_m = 137$ μH.

A 200 nm PECVD SiO_2 and 100 nm dc sputtered Al were deposited for the dielectric layer and top metal layer of the metasurfaces, respectively. The Al layer was patterned and etched using a DPS etch system to form the patterned nanostructures of the metasurface. Subsequently, vias to the top electrode of the resonator were formed by ICP-RIE. The shape of the AlN resonator body was defined by first etching the SiO_2 and then etching the AlN using the same patterning. Finally, the resonators were released from the substrate using an XeF_2 etch. Overall, this methodology enabled the fabrication of a 6″ wafer containing 17 repeating 2.2 × 2.7 cm chips, with each chip containing ∼2000 IR detectors of which 720 are reported here. The process can be easily altered to be made CMOS compatible and is integrable through either heterogeneous or monolithic processes.

Fig. 2(a) shows an SEM image of an individual device, including details of the metasurface unit cell (bottom-left) and the resonator anchors (bottom-right). Fig. 2(b) shows an optical image of the fabricated 2.2 × 2.7 cm chip.

III. Measurement and Discussion

The characterization of IR detectors requires three different types of measurements: 1) IR absorption, to determine the IR absorption profile of each sensor; 2) RF response, to determine the device behavior in terms of quality factor, RF operation frequency, and fluctuation induced noise; and 3) RF/IR sensing metrics, to determine sensing parameters such as NEP and responsivity. As described below, an automated characterization system has been developed to characterize the RF response and IR sensing performance of the detectors in an effective manner.

The IR absorption spectra of the devices were characterized using a Bruker Fourier transform IR (FTIR) spectrometer coupled to a Hyperion 2000 microscope. The reflection spectra R was measured with the FTIR, and the absorption was calculated as $A = 1 - R$, assuming that there was no transmission through the metasurface due to the metal ground plane, which has a thickness much larger than the penetration depth of IR light. Fig. 4 shows measured absorption spectra from 6 of the 20 metasurface designs considered in this study. Results from other metasurface configurations are summarized in Table I. The measured absorption spectra for a set of devices decorated with metasurfaces composed of 1) patch unit-cells, with patch width and length $a = b = 1.11$, 1.14, and 1.17 μm and period $P = 3.5$ μm and 2) cross-shaped unit cells, with cross width $a = 350$ nm, cross length $b = 2.17$, 2.2, and 2.23 μm, and period $P = 3.5$ μm, are shown in Fig. 4. Results show several devices achieving an absorption of 95% at $\lambda \sim 5.3$ μm, with a FWHM of ∼450 nm, demonstrating that strong and spectrally selective mid-IR absorption can be readily achieved with optical lithography processes. For each RF MEMS resonator with defined geometrical dimensions, 20 repetitions were fabricated within the chip shown in Fig. 2(b). Each of these resonators was decorated with a different metasurface. These structures, which exhibit an IR absorption profile similar to the ones shown in Fig. 4, were designed to be centered around 4 and 5.5 μm, with small geometrical variations in the nano-resonators that compose

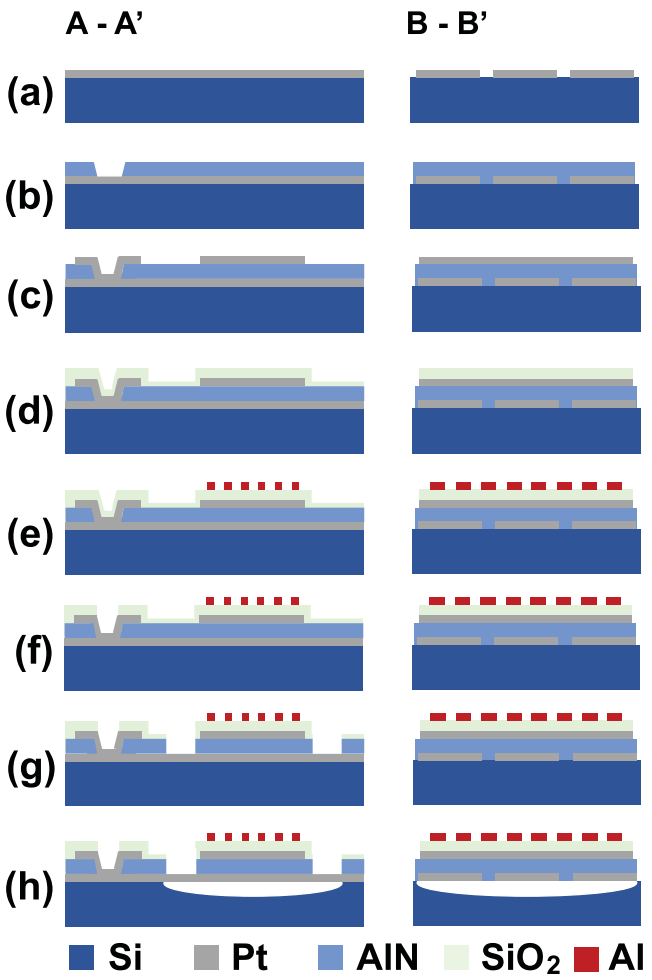

Fig. 3. Microfabrication process for the IR detector, consisting of (a) patterning and deposition of the 100 nm Pt bottom electrode, (b) deposition of 1 μm piezoelectric AlN layer followed by patterning and dry etch for via to bottom electrode, (c) patterning and deposition of the 100 nm Pt top electrode/metasurface ground layer, (d) deposition of 200 nm SiO_2, (e) deposition, patterning and etch of 100 nm Al to form the metasurface nanostructures, (f) patterning and etch of SiO_2 for via to top electrode, (g) patterning and subsequent SiO_2 and AlN etched to define resonator shape, and (h) isotropic Xenon Difluoride etch to release resonators from substrate.

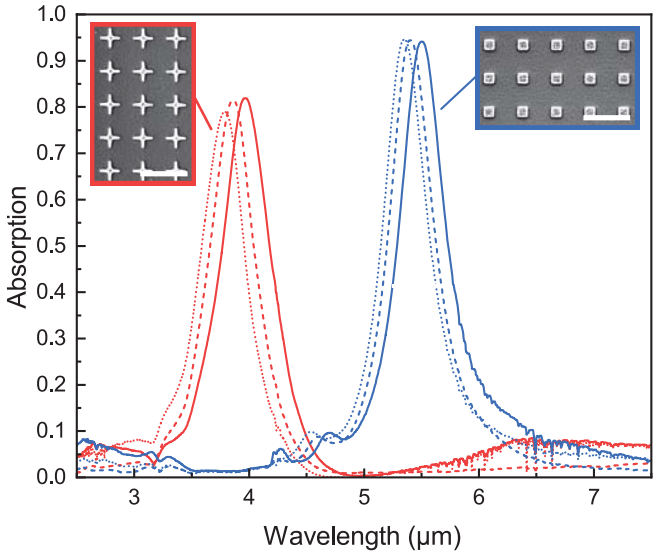

Fig. 4. Measured absorption spectra of some of the fabricated IR sensors. Each device is decorated with a metasurface targeting *a* specific wavelength. For instance, metasurfaces centered around 5.5 μm (blue lines) are composed of patch unit cells with a side of $a = b = 1.11$, 1.14, and 1.17 μm going from left to right, and a period = 3.5 μm (metasurface # 1, 2, 3, respectively, in Table I). Metasurfaces centered around 4 μm (red lines) are composed of cross-shaped unit cells with $a = 350$ nm, $b = 2.17$, 2.2, and 2.23 μm going from left to right, and period = 3.5 μm (metasurface # 13, 14, 15, respectively, in Table I). [Inset: SEM images of patch and cross-shaped nanostructures that conform to the metasurfaces (scale bar is 5 μm)].

their unit-cell geometries. The goal of this study is to assess the capabilities of DUV lithography and its effect on the overall IR sensors. As seen from Table I, lithography variations as small as 30 nm can be fabricated and distinguished in the absorbance measurements, implying highly spectrally selective detection capabilities. IR absorption measurements were performed over identical metasurface structures printed on top of the 36 different types of MEMS devices considered in this study, leading to overlapping absorption profiles; this expected response appears because the ground plane/top electrode effectively isolates the metasurface from the MEMS body. Results confirmed that absorption profiles >90% can be obtained at desired wavelengths while keeping FWHM ~500 nm. It should be noted that the FWHM can also be controlled by changing the type of unit cell that composes the metasurface [26]. In general, the type of metasurface will depend on the final application of the IR detector and may provide IR spectral selectivity, as demonstrated here, useful for targeting specific fingerprints in the IR typical of gases [29] and molecules [30]; wide IR absorption, useful to detect a large range of IR signals [31]; and even polarization dependent IR absorption [32], useful to accurately detect chiral molecules [33].

The potential influence of the metasurface on the sensor response was assessed by measuring the MEMS resonance frequency. Within the sets of 36 resonators, the coefficient of variation (ratio of standard deviation to mean) of the resonance has been calculated as ~0.1%, indicating a low level of dispersion around the mean. Some level of variation is expected as the anchor dimensions have some effect on the resonance frequency [25]. Comparing the mean resonance frequency of each set of MEMS devices decorated with a different metasurface design, the coefficient of variation of the resonance frequency is 35%, indicating more variation. One-way ANOVA analysis [34] produces a p-value of 270, confirming that the mean resonance frequencies are significantly different. However, comparing the resonance frequencies with the metasurface mass, no trend was observed. It should be noted that the MEMS resonance frequency can be affected by other factors such as AlN uniformity, which might vary across the chip, fabrication tolerances, or environmental fluctuations in the lab during measurements.

The RF response and IR sensing performance of the detectors were characterized using a home-made automated system composed of 1) a ground signal ground (GSG) RF probe able to make an electrical connection with a device; 2) a step-motor to drive the probe landing/retracting; 3) a motorized high-precision 2-D translation stage to select individual devices,

coupled to a 3-D printed vacuum chuck to securely adhere the chip to the stage; 4) a VNA (Copper Mountain TR1300) to perform electrical measurements; 5) a motorized linear stage holding optical components to collimate and focus the IR beam on the chip; and 6) a blackbody radiator (HGH IR RCN Series). The optical components can be moved in and out of the IR beam path by the linear stage, allowing control over the incident radiation on the device under test. This system was employed to characterize the 2.2 × 2.7 cm chip shown in Fig. 2(b).

First, the electrical characterization of the resonators was carried out using the VNA calibrated using a standard short-open-load substrate at room temperature and atmospheric pressure. Fig. 2(c) shows the admittance response of a specific device with anchor width $W_a = 15$ μm and anchor length $L_a = 12$ μm. The resonance frequency of the resonator was measured as ~208 MHz. A modified Butterworth-Van Dyke (MBVD), (see inset of Fig. 2(c)] circuit was employed to model the MEMS resonator in terms of a motional resistance (R_m), capacitance (C_m), and inductance (L_m) connected in series in a branch, that is in parallel with an electrical capacitance (C_0) and resistance (R_0) [35]. The circuit model allows the extraction of the resonator quality factor Q as $Q = 1/2\pi f_s C_m R_m = 2\pi f_s L_m / R_m$ and the electromechanical coupling coefficient k_t^2 as $k_t^2 = \pi^2 C_m / 8C_0$. Devices with quality factors of ~2220 and electromechanical coupling of ~2.02% have been measured, leading to a high figure of merit of $k_t^2 \cdot Q = 44.8$. Such metrics are comparable to Q and k_t^2 values reported for common AlN CMR devices [24], indicating that the mechanical damping from the additional oxide and metal layer making up the PMA was not dominant in terms of the resonator performance. Fig. 5(a) shows the distribution of the measured quality factor of devices with varying anchor dimensions, calculated from Y-parameter measurements as $Q = f_s / f_{3\,\mathrm{dB}}$ [35]. The trend was found to be independent of the anchor length, thus only $L_a = 12$ μm is plotted. The quality factor shows an increasing trend with increasing anchor width until reaching a maximum at $W_a = 15$ μm, before decreasing for larger anchor widths. One-way ANOVA analysis [34] provided a p-value of 25.7, confirming the population means are significantly different. A maximum average quality factor of ~2250 was obtained. These findings are in line with what was previously reported in [24] and show that the presence of the metasurface does not significantly modify the CMR response. For the rest of the analysis, only detectors with a quality factor larger than 250 are considered.

The fluctuation-induced noise f_n of the detectors was extracted through the short-term frequency instability at a frequency of 100 Hz. This measurement was carried out by exciting each detector with a continuous wave from the VNA at the frequency of the maximum slope of the magnitude of the admittance curve, as detailed in [17]. The root mean square (rms) amplitude noise was extracted from this measurement by taking the standard deviation, which was then converted into frequency noise by dividing it by the slope. Subsequently, the frequency noise spectral density was found by dividing by the square root of the measurement

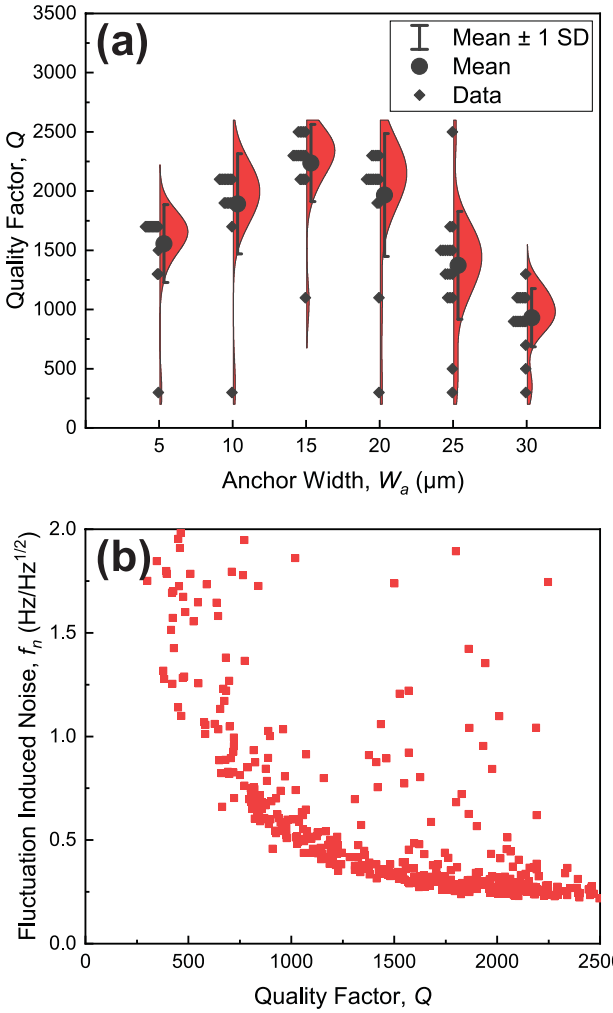

Fig. 5. (a) Distribution of measured quality factor of resonators with varying anchor width dimensions at an anchor length of $L_a = 12$ μm (number of data points = 106 out of 120). The mean, standard deviation, and density of data are shown. One-way ANOVA analysis [34] provides a p-value of 25.7, confirming the population means are significantly different (at the 0.05 level). (b) Spectral noise density of resonators at an offset frequency of 100 Hz versus measured quality factor (number of data points = 472 out of 720), demonstrating a decreasing trend.

bandwidth (100 Hz). Fig. 5(b) shows the fluctuation-induced noise plotted as a function of the quality factor. Only fluctuation-induced noise below 2 Hz/$\sqrt{\text{Hz}}$ was considered, a threshold that was imposed to eliminate outlier responses. It was found that the fluctuation-induced noise follows a power law dependency with the quality factor. Up to a quality factor of ~1000, improvement in the quality factor leads to a significant improvement in the fluctuation-induced noise; beyond this, the fluctuation-induced noise saturates with the Q-factor at a minimum noise level. The absolute lowest f_n within the measured group of data was obtained as 0.218 Hz/$\sqrt{\text{Hz}}$ with a corresponding quality factor of ~2500. Fluctuation-induced noise within 10% of the lowest measured noise can be obtained for quality factors as low as 1800, which provides a larger design space for anchor widths when optimizing the resonator performance. This extends the power law effect of damping on flicker noise revealed in [36] for 1 GHz CMRs. Our study includes a larger data set of CMR devices loaded with metasurfaces, which may facilitate revealing such a trend.

It should also be noted that the noise coming from the VNA source is included in our results. Moreover, we are not differentiating here between pure amplitude fluctuations (e.g., due to variable Q), and amplitude variations due to frequency fluctuations. Even though more meticulous noise studies may be performed using a modified homodyne measurement setup and employing a signal source analyzer to determine amplitude and phase noise [37], these studies are usually cumbersome and tedious and cannot be readily applied to explore the response of thousands of devices.

The sensing performance of the IR detectors is demonstrated in terms of responsivity and NEP. To this purpose, IR waves from the blackbody radiator were collimated and focused onto the device under test using a combination of BaF_2 lenses and mirrors. To minimize potential drifts between measurements, the characterization of each individual device was performed without and with IR illumination back-to-back, utilizing the motorized linear stage that moves the optics in or out in a span of a few seconds. Prior to the measurements, the IR power emitted by the blackbody radiator at 1350 °C and focused on the device plane was characterized using a mercury-cadmium-telluride photodetector (Thorlabs PDAVJ10). Then, the spectral power distribution of the received power was resolved by applying Planck's blackbody law [38]. This calibration approach permits the determination of the spectral power distribution of the IR exciting the device under test.

The responsivity of the IR detector is calculated as the resonance frequency shift induced in the device by the incoming IR light divided by the total IR power absorbed, expressed as $R_s = \Delta f / P_{\mathrm{IR}}$. In this equation, Δf is the frequency shift generated in the device under IR illumination [see inset of Fig. 6(a)] and P_{IR} is the IR power absorbed by the device, calculated as $P_{\mathrm{IR}} = \int Q_p(\lambda)\eta(\lambda)d\lambda$. Here, $Q_p(\lambda)$ is the incident IR power versus wavelength, and η is the metasurface IR absorption profile. It should be stressed that the absorption profile is employed here to normalize responsivity, aiming to decouple the device performance and the spectral profile of the IR source. This normalization is needed when broadband thermal IR sources are employed to characterize the sensors, as in this work. Even though such sources emit broadband light over the entire IR spectrum, following Planck's blackbody law [38], only a limited subset of these waves—defined by the metasurface absorption profile—will effectively interact with the device. This is equivalent to considering that the device is illuminated with IR light oscillating at the wavelengths defined by the metasurface absorption profile. To further understand this scenario, let us consider two identical MEMS sensors decorated with metasurfaces that target 5 μm but exhibit different FWHMs of 500 nm and 1 μm, respectively. If we consider the P_{IR} as the total power radiated by the blackbody radiator, the responsivity of the device with higher FWHM will be significantly larger. However, if we consider the actual IR power absorbed by these structures, both sensors will lead to similar responsivities—which better capture their transduction mechanism. Finally, it must be noted that the most accurate responsivity metric should be wavelength-dependent, i.e., $R_s(\lambda) = \Delta f / P_{\mathrm{IR}}(\lambda)$. However, determining such a metric would require a broadband and coherent IR laser (like those based on optical parameter oscillators [39]) not available for this study.

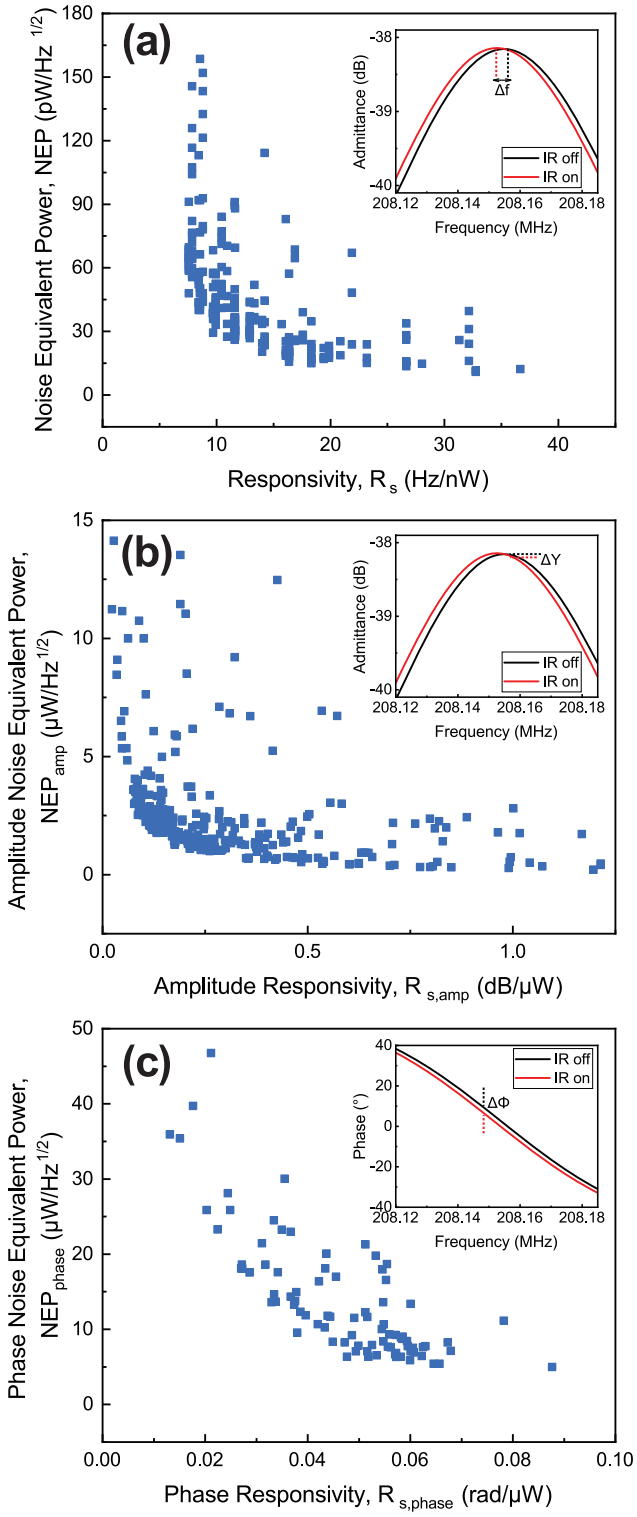

Fig. 6. Calculated NEP versus responsivity for the IR devices for different interrogation mechanisms, namely (a) frequency shift (number of data points = 369 out of 720), (b) amplitude shift (number of data points = 339 out of 720), and (c) phase shift (number of data points = 144 out of 720). Insets respectively show frequency, amplitude, and phase shift for a device with $Q = 2220$ ($W_a = 15$ μm, $L_a = 12$ μm) without and with IR excitation, demonstrating frequency shift of 3.750 kHz as well as variations in amplitude and phase.

The inset of Fig. 6(a) shows that the measured frequency shift for the device for which RF measurements are presented in Fig. 2(c) is 3.750 kHz. This device exhibits a quality factor of $Q = 2220$, has anchors with dimensions $W_a = 15\ \mu$m, $L_a = 12\ \mu$m, and hosts a metasurface loaded with nanoresonators with $a = 450$ nm, $b = 2.2\ \mu$m, and period $= 3.5\ \mu$m (metasurface #17). The corresponding responsivity was calculated as 18.3 Hz/nW. For the 36 MEMS resonators that have different anchor dimensions but are loaded with the same metasurface, the mean and standard deviation of the responsivity were obtained as 26.0 and 13.9 Hz/nW, respectively, resulting in a coefficient of variation of 53%. Similar numbers were obtained for the other metasurface designs, indicating notable variation in the responsivity with anchor dimensions. Previous works [17] and [18] have approximated the relationship between the responsivity and the device geometry and material properties as $R_s = \eta \cdot R_{\text{th}} \cdot \text{TCF} \cdot f_0$, where R_{th} is the thermal resistance, TCF is the temperature coefficient of frequency of the piezoelectric resonator (typically -30 ppm/K for AlN films with thickness $\leq 1\ \mu$m [40]). Thermal resistance was approximated using $R_{\text{th}} = L_a/W_a(\kappa_{\text{Pt}}h_{\text{Pt}} + \kappa_{\text{AlN}}h_{\text{AlN}} + \kappa_{\text{SiO}_2}h_{\text{SiO}_2})$, where κ is the material thermal conductivity and h is the material thickness in the Pt/AlN/SiO_2 stack making up the resonator anchors, through which heat escapes [41]. Exploring all anchor dimensions employed in the fabricated devices, thermal resistances in the range of 3.8 to 108 K/mW were obtained for the 36 resonators. Measured responsivities did not reveal a conclusive trend with thermal resistance. We suspect that reaching a definite conclusion would require using a coherent IR laser to illuminate the devices and to increase the number of structures; additionally, it should be noted that the equation employed to define R_{th} is an approximation that might not hold for all the scenarios considered here. Comparing the different metasurface designs to one another, and considering all MEMS devices, one-way ANOVA yielded a p-value of 9.7 at the 0.05 level, indicating that the mean responsivity obtained for the different metasurface designs are statistically different. This further supports spectral selectivity, and that the 30 nm lithography variation achieved with DUV lithography that can be distinguished in FTIR measurements also can be distinguished in responsivity measurements. Additionally, the thermal resistance R_{th} has not been analyzed across metasurface designs, as the responsivity definition is not wavelength dependent, and thus such comparison would not be relevant. Finally, there was no clear trend between the metasurface measured peak absorption wavelength, peak absorption, or FWHM with measured responsivity, indicating that metasurface designs can be targeted for spectral selectivity in the mid-IR with no loss of performance.

In addition to the common definition of responsivity based on frequency shift for this type of integrated MEMS/metasurface detectors, we introduce here two alternative approaches to obtain the device responsivity that is associated with the change induced in the amplitude and phase of an RF signal that excites the device. This leads to a responsivity in amplitude, $R_{s,\text{amp}} = \Delta Y/P_{\text{IR}}$, and phase, $R_{s,\text{phase}} = \Delta\phi/P_{\text{IR}}$, defined as the change in the amplitude and phase of the device Y parameter at resonance versus IR light. Insets in Fig. 6(b) and (c) show the amplitude and phase of the measured admittance parameters with and without IR radiation, for the device with RF measurements shown in Fig. 2(c). The amplitude/phase shift was extracted at frequency of maximum variation between the response without and with IR. Maximum amplitude variation was achieved at 208.11063 MHz, and the maximum phase variation is achieved at 208.15125 MHz, indicating that separate responsivities can be defined for amplitude and phase, presenting alternative interrogation scheme possibilities for increased accuracy or redundancy. These amplitude and phase definitions also enable the use of alternative detection mechanisms than a VNA, such as gain detection or homodyne detection, enabling easier or more compact detection circuitry.

Based on these responsivity definitions, corresponding NEPs were calculated and compared. Fig. 6 shows the NEP as a function of the responsivity, for the frequency, amplitude, and phase definitions. As shown in Fig. 6(a), the NEP calculated from the noise-induced frequency fluctuation f_n divided by the responsivity of the detector, NEP $= f_n/R_s$, shows a reverse power law trend with the responsivity, i.e., responsivity and NEP improve together. Remarkably, our study demonstrated that NEP as low as 11 pW/$\sqrt{\text{Hz}}$ can be obtained with this technology. The amplitude noise spectral density was extracted from the intermediate step of the fluctuation-induced noise density calculation, and the corresponding NEP is defined as $\text{NEP}_{\text{amp}} = Y/R_{s,\text{amp}}$. The phase noise spectral density was obtained by conversion from the fluctuation-induced noise density as $\phi = f_n/f$, where $\phi(\text{rad}/\sqrt{\text{Hz}})$ is the phase noise spectral density, $f_n(\text{Hz}/\sqrt{\text{Hz}})$ is the frequency fluctuation spectral density, and f is the offset frequency [42] (100 Hz in this case). The resulting NEP is given by $\text{NEP}_{\text{phase}} = \phi/R_{s,\text{phase}}$. The definitions based on amplitude shift and phase shift demonstrated similar inverse relationships between responsivity and NEP, indicating that these can successfully be used as alternate interrogation schemes. As a clear trend with detector geometry was not observed for responsivity, we can infer that the NEP is limited by the fluctuation-induced noise. Thus, for best NEP performance, the resonator should be designed to provide the lowest fluctuation-induced noise. The range of values of the NEP and responsivity respectively for the amplitude- and phase-based definition; however, are narrower compared to the standard frequency-based detection, indicating a narrower dynamic range. This flexibility is valuable in applications where the strength of the signal can vary significantly. Even though amplitude and phase interrogation techniques lead to significantly higher NEP than the common frequency-shift approach, these schemes may benefit from dedicated readout circuits that will enhance the overall detector performance.

For high-resolution (low NEP) and high selectivity (responsivity) devices, the design of the MEMS and metasurfaces can be decoupled. The spectral responsivity of IR detectors is key in indicating their sensitivity to different wavelengths within the IR spectrum. Detectors with a broad spectral responsivity can be more versatile in applications where various types of IR radiation need to be detected, whereas a narrowband response

such as studied in this work is preferred for spectral selectivity, in applications where differentiation between signals or labeling is required. The selectivity of the IR detector can be tuned through the metasurface design, with the peak absorption of the wavelength determining the spectral response and the FWHM determining the band of response. High responsivity in IR detectors translates to increased detection sensitivity. Detectors that efficiently convert incident IR radiation into electrical signals provide more accurate and reliable measurements, even at lower levels of radiation. Theoretically, the sensor responsivity is directly proportional to the thermal resistance of the resonators, which relates directly to the anchor dimensions of the resonator. However, the experimental study shown in this work has not revealed a clear trend, thus more investigation is necessary to clarify this point. IR detection has a wide breadth of potential applications, ranging from areas like industrial process monitoring [43], medical diagnostics [44], to astronomy [45], all of which may require specific responsivity characteristics. Customized responsivity profiles, as enabled through the frequency, amplitude, or phase detections schemes can allow IR detectors to excel in specialized applications. The NEP sets a fundamental limit on the lowest detectable signal power for an IR detector. It serves as a benchmark for understanding the capabilities of the detector and can be a critical factor in designing systems with optimal performance. Different applications, such as astronomy [45], medical imaging [44], or environmental monitoring [46], may have specific NEP requirements. Tailoring the NEP to meet the demands of specific applications ensures optimal performance and reliable data. For best NEP, the fluctuation induced noise should be minimized. This requires tuning the anchor dimensions properly, but not necessarily to the highest quality factor, which provides flexibility in terms of the anchor dimensions and can therefore simplify the fabrication.

The approaches in this study enabled the fabrication and characterization of a large number of MEMS/metasurface IR detectors, which we have used to enlighten the design process of these on the device level. This approach also enables yield analysis, which was not carried out here as it is out of the scope of the study but is nevertheless a crucial step in the scope of scaling up technologies for mass production. As a technology, MEMS/metasurface IR sensors still face unexplored aspects such as reliability, calibration, packaging, integration with read-out circuitry, and signal processing complexities. Addressing these challenges presents opportunities for innovation and research to further enhance the performance and reliability of MEMS/metasurface IR sensors and explore the full potential of these promising devices.

IV. Conclusion

This article has provided a comprehensive experimental study of uncooled IR detectors based on integrated RF AlN CMR with spectrally selective IR metasurfaces. Hundreds of IR sensors have been fabricated, enabled by an optimized optical lithography process to pattern metasurfaces on MEMS, and then characterized using a dedicated testing system. A large array of metrics, including RF quality factor, fluctuation-induced noise, responsivity, and NEP, has been collected and analyzed. Our analysis has revealed that the metasurface and resonator designs can be decoupled to meet IR responsivity and NEP specifications, respectively. The metasurface design can be tailored to target the desired IR spectral range and selectivity, whereas the MEMS body can be tailored to minimize the noise and enhance the device's RF quality factor. Measured data confirms that the quality factor can be maximized for optimal anchor widths, which is a trend that is somewhat independent of the anchor length. Additionally, the frequency fluctuation-induced noise displays a decreasing power law trend with a larger RF quality factor. As a result, maximizing the quality factor is not a critical rule necessary for optimized fluctuation-induced noise. Such guidelines relax the fabrication process and provide a larger design space for the development of IR sensors with optimized NEP. Additionally, alternative definitions for responsivity and NEP based on amplitude and phase detection are presented and compared to those obtained through the common frequency shift in the resonators. Even though the performance measured with these metrics is not optimal, they may enable new readout circuits and interrogation approaches. Our work demonstrates NEP in the low $\mathrm{pW}/\sqrt{\mathrm{Hz}}$ and provides new guidelines for the implementation of improved integrated MEMS/metasurface uncooled IR detectors, with applications in field ranging from healthcare and astronomy to communications, spectroscopy, and sensing.

Acknowledgment

The authors would like to thank Zhixing Lin and Arnau Cluet for their help with the measurement setup. Part of this study was carried out at the UC Davis Center for Nano and Micro Manufacturing (CNM2) and UC Berkeley Marvell Nanofabrication Laboratory.

References

[1] A. Rogalski, "History of infrared detectors," *Opto-Electron. Rev.*, vol. 20, no. 3, pp. 279–308, Jan. 2012.
[2] R. K. Bhan and V. Dhar, "Recent infrared detector technologies, applications, trends and development of HgCdTe based cooled infrared focal plane arrays and their characterization," *Opto-Electron. Rev.*, vol. 27, no. 2, pp. 174–193, Jun. 2019.
[3] C. Corsi, "History highlights and future trends of infrared sensors," *J. Modern Opt.*, vol. 57, no. 18, pp. 1663–1686, Oct. 2010, doi: 10.1080/09500341003693011.
[4] A. Rogalski, "Graphene-based materials in the infrared and terahertz detector families: A tutorial," *Adv. Opt. Photon.*, vol. 11, no. 2, pp. 314–319, 2019.
[5] H. Wang and D. H. Kim, "Perovskite-based photodetectors: Materials and devices," *Chem. Soc. Rev.*, vol. 46, no. 17, pp. 5204–5236, 2017.
[6] A. D. Stiff-Roberts, "Quantum-dot infrared photodetectors: A review," *J. Nanophotonics*, vol. 3, no. 1, Apr. 2009, Art. no. 031607.
[7] A. Rogalski, M. Kopytko, and P. Martyniuk, "Two-dimensional infrared and terahertz detectors: Outlook and status," *Appl. Phys. Rev.*, vol. 6, no. 2, Jun. 2019, Art. no. 021316.
[8] V. J. Gokhale and M. Rais-Zadeh, "Uncooled infrared detectors using gallium nitride on silicon micromechanical resonators," *J. Microelectromech. Syst.*, vol. 23, no. 4, pp. 803–810, Aug. 2014.
[9] M. B. Pisani, K. Ren, P. Kao, and S. Tadigadapa, "Application of micromachined Y-cut-quartz bulk acoustic wave resonator for infrared sensing," *J. Microelectromech. Syst.*, vol. 20, no. 1, pp. 288–296, Feb. 2011.
[10] M. Z. Koohi and A. Mortazawi, "BST thin film bulk acoustic resonator optimization for un-cooled IR sensors application," in *Proc. 47th Eur. Microw. Conf. (EuMC)*, Oct. 2017, pp. 328–330.

[11] A. Islam, J. Lee, and P. X.-L. Feng, "Black phosphorus NEMS resonant infrared (IR) detector," in *Proc. IEEE 33rd Int. Conf. Micro Electro Mech. Syst. (MEMS)*, Mar. 2020, pp. 826–829.
[12] Z. Qian, Y. Hui, F. Liu, S. Kang, S. Kar, and M. Rinaldi, "Graphene-aluminum nitride NEMS resonant infrared detector," *Microsystems Nanoeng.*, vol. 2, pp. 1–7, Jun. 2016.
[13] M. A. Noginov and V. A. Podolskiy, *Tutorials in Metamaterials*. Boca Raton, FL, USA: CRC Press, 2011.
[14] P. K. Choudhury, *Metamaterials: Technology and Applications*. Boca Raton, FL, USA: CRC Press, 2021.
[15] N. I. Landy, S. Sajuyigbe, J. J. Mock, D. R. Smith, and W. J. Padilla, "Perfect metamaterial absorber," *Phys. Rev. Lett.*, vol. 100, no. 20, May 2008, Art. no. 207402.
[16] Y. Hui and M. Rinaldi, "High performance NEMS resonant infrared detector based on an aluminum nitride nano-plate resonator," in *Proc. 17th Int. Conf. Solid-State Sensors, Actuat. Microsystems*, Jun. 2013, pp. 968–971.
[17] Y. Hui, J. S. Gomez-Diaz, Z. Qian, A. Alu, and M. Rinaldi, "Plasmonic piezoelectric nanomechanical resonator for spectrally selective infrared sensing," *Nature Commun.*, vol. 7, no. 1, p. 11249, Apr. 2016.
[18] Y. Hui, S. Kang, Z. Qian, and M. Rinaldi, "Uncooled infrared detector based on an aluminum nitride piezoelectric fishnet metasurface," *J. Microelectromech. Syst.*, vol. 30, no. 1, pp. 165–172, Feb. 2021.
[19] J. Tao et al., "Dual functionality metamaterial enables ultra-compact, highly sensitive uncooled infrared sensor," *Nanophotonics*, vol. 10, no. 4, pp. 1337–1346, Feb. 2021.
[20] X. Tan et al., "Non-dispersive infrared multi-gas sensing via nanoantenna integrated narrowband detectors," *Nature Commun.*, vol. 11, no. 1, p. 5245, Oct. 2020.
[21] Z. Qian, S. Kang, V. Rajaram, and M. Rinaldi, "Narrowband MEMS resonant infrared detectors based on ultrathin perfect plasmonic absorbers," in *Proc. IEEE SENSORS*, Oct. 2016, pp. 1–3.
[22] Y. Hou, M. Zhang, G. Han, C. Si, Y. Zhao, and J. Ning, "A review: Aluminum nitride MEMS contour-mode resonator," *J. Semiconductors*, vol. 37, no. 10, Oct. 2016, Art. no. 101001.
[23] G. Piazza, P. J. Stephanou, and A. P. Pisano, "Piezoelectric aluminum nitride vibrating contour-mode MEMS resonators," *J. Microelectromech. Syst.*, vol. 15, no. 6, pp. 1406–1418, Dec. 2006.
[24] J. Segovia-Fernandez, M. Cremonesi, C. Cassella, A. Frangi, and G. Piazza, "Experimental study on the impact of anchor losses on the quality factor of contour mode AlN resonators," in *Proc. 17th Int. Conf. Solid-State Sensors, Actuat. Microsystems*, 2013, pp. 2473–2476.
[25] J. Segovia-Fernandez and G. Piazza, "Analytical and numerical methods to model anchor losses in 65-MHz AlN contour mode resonators," *J. Microelectromech. Syst.*, vol. 25, no. 3, pp. 459–468, Jun. 2016.
[26] S. Kang, Z. Qian, V. Rajaram, S. D. Calisgan, A. Alu, and M. Rinaldi, "Ultra-Narrowband metamaterial absorbers for high spectral resolution infrared spectroscopy," *Adv. Opt. Mater.*, vol. 7, no. 2, Jan. 2019, Art. no. 1801236.
[27] N. To, S. Juodkazis, and Y. Nishijima, "Detailed experiment-theory comparison of mid-infrared metasurface perfect absorbers," *Micromachines*, vol. 11, no. 4, p. 409, Apr. 2020.
[28] X. Lu, T. Zhang, R. Wan, Y. Xu, C. Zhao, and S. Guo, "Numerical investigation of narrowband infrared absorber and sensor based on dielectric-metal metasurface," *Opt. Exp.*, vol. 26, no. 8, pp. 10179–10187, 2018.
[29] D. Popa and F. Udrea, "Towards integrated mid-infrared gas sensors," *Sensors*, vol. 19, no. 9, p. 2076, May 2019.
[30] R. Eischens and W. Pliskin, "The infrared spectra of adsorbed molecules," in *Advances in Catalysis*, vol. 10. Amsterdam, The Netherlands: Elsevier, 1958, pp. 1–56.
[31] W. Guo, Y. Liu, and T. Han, "Ultra-broadband infrared metasurface absorber," *Opt. Exp.*, vol. 24, no. 18, pp. 20586–20592, Sep. 2016.
[32] Y. Sun et al., "Switchable bifunctional metasurface based on VO_2 for ultra-broadband polarization conversion and perfect absorption in same infrared waveband," *Opt. Commun.*, vol. 503, Jan. 2022, Art. no. 127442.
[33] M. S. Mahmud, D. Rosenmann, D. A. Czaplewski, J. Gao, and X. Yang, "Chiral plasmonic metasurface absorbers in the mid-infrared wavelength range," *Opt. Lett.*, vol. 45, no. 19, pp. 5372–5375, 2020.
[34] L. Stahle and S. Wold, "Analysis of variance (ANOVA)," *Chemometrics Intell. Lab. Syst.*, vol. 6, no. 4, pp. 259–272, Nov. 1989.
[35] J. D. Larson, P. D. Bradley, S. Wartenberg, and R. C. Ruby, "Modified Butterworth-Van Dyke circuit for FBAR resonators and automated measurement system," in *Proc. IEEE Ultrason. Symp.*, Oct. 2000, pp. 863–868.
[36] A. Lozzi, E. Ting-Ta Yen, P. Muralt, and L. G. Villanueva, "$Al_{0.83}Sc_{0.17}N$ contour-mode resonators with electromechanical coupling in excess of 4.5%," *IEEE Trans. Ultrason., Ferroelectr., Freq. Control*, vol. 66, no. 1, pp. 146–153, Jan. 2019.
[37] H. J. Kim, J. Segovia-Fernandez, and G. Piazza, "The impact of damping on flicker frequency noise of AlN piezoelectric MEMS resonators," *J. Microelectromech. Syst.*, vol. 26, no. 2, pp. 317–324, Apr. 2017.
[38] G. B. Rybicki and A. P. Lightman, *Radiative Processes in Astrophysics*. Hoboken, NJ, USA: Wiley, 1991.
[39] S. E. Harris, "Tunable optical parametric oscillators," *Proc. IEEE*, vol. 57, no. 12, pp. 2096–2113, Dec. 1969.
[40] J. H. Kuypers, C.-M. Lin, G. Vigevani, and A. P. Pisano, "Intrinsic temperature compensation of aluminum nitride Lamb wave resonators for multiple-frequency references," in *Proc. IEEE Int. Freq. Control Symp.*, May 2008, pp. 240–249.
[41] J. Segovia-Fernandez, "Damping and nonlinearities in aluminum nitride contour mode resonators," Doctor of Philosophy, Elect. Comput. Eng., Carnegie Mellon Univ., Pittsburgh, PA, USA, 2015.
[42] E. Rubiola and F. Vernotte, "The companion of Enrico's chart for phase noise and two-sample variances," *IEEE Trans. Microw. Theory Techn.*, vol. 71, no. 7, pp. 2996–3025, Jul. 2023.
[43] P. Martin and R. Holdsworth, "High-resolution infrared spectroscopy for in situ industrial process monitoring," *Spectrosc. Eur.*, vol. 16, pp. 8–15, Oct. 2004.
[44] L. Jiang et al., "A perspective on medical infrared imaging," *J. Med. Eng. Technol.*, vol. 29, pp. 257–267, Jan. 2005.
[45] G. H. Rieke, "Infrared detector arrays for astronomy," *Annu. Rev. Astron. Astrophys.*, vol. 45, no. 1, pp. 77–115, Sep. 2007.
[46] P. D. LeVan and U. Sakoglu, "Infrared sensing technologies assisting environmental monitoring," *Proc. SPIE*, vol. 11503, pp. 38–49, Aug. 2020.

Melisa Ekin Gülseren (Member, IEEE) received the B.S. and M.S. degrees in electrical and electronics engineering from Bilkent University, Ankara, Turkey, in 2016 and 2019, respectively. She is currently pursuing the Ph.D. degree in electrical and computer engineering from the University of California, Davis, CA, USA.

Her research interests include MEMS/NEMS devices, metamaterials, and micro-/nano-fabrication.

Matthew Benson was born in Los Angeles, CA, USA. He received the B.S. degree in electrical engineering from the University of California, Davis, CA, USA, in 2021, where he is currently pursuing the Ph.D. degree in electrical engineering.

His research interests include the areas of infrared and terahertz sensing, MEMS/NEMS devices, and metamaterials.

Ryan W. Parker was born in San Diego, CA, USA, in 1997. He received the B.S. and M.S. degrees in electrical engineering from the University of California, Davis, CA, USA, in 2023.

From 2021 to 2023, he was a Student Researcher at the Applied Micro/Nano Electromagnetics Research Laboratory. Since 2023, he was been a Product Design Engineer at Texas Instruments Inc. (RFAB), Dallas, TX, USA.

Jeronimo Segovia-Fernandez (Member, IEEE) received the Ph.D. degree in electrical and computer engineering from Carnegie Mellon University, Pittsburgh, PA, USA, in 2015.

He is a member and Group Technical Staff (MGTS) at Texas Instruments Kilby Labs, Santa Clara, CA, USA, and a Visiting Lecturer with the University of California, Berkeley, CA, USA. He has authored/coauthored more than 50 journals and conference publications and invented/co-invented more than 15 patents (seven of them awarded). His main research interests include piezoelectric MEMS integrated with analog and RF circuits for applications related to wireless communications, timing, sensing, and power electronics.

Dr. Segovia-Fernandez received the IEEE Sensors Council Technical Achievement and the SCV Outstanding Engineer Awards in 2023, the SRC Outstanding Industry Liaison Award in 2022, and the IFCS Best Student Paper Award in 2013. He is a technical reviewer for several IEEE and MDPI journals, a TPC Member for IFCS and Transducers, and volunteers as the Chair of the IEEE SFBA MEMS and Sensors Chapter, and Publicity VP of IEEE MEMS-TC.

Ernest Ting-Ta Yen (Member, IEEE) received the double B.S. degree in electrical engineering and power mechanical engineering from National Tsing Hua University, Hsinchu, Taiwan, in 2004, the M.S. degree in electrical engineering from the University of California, Berkeley, CA, USA, in 2012, and the Ph.D. degree in mechanical engineering from the University of California, Berkeley, in 2012.

He joined the Kilby Labs–Texas Instruments, Santa Clara, CA, USA, as a MEMS Technologist. His research interests include piezoelectric MEMS in RF and sensing applications. He developed the dual-Bragg acoustic resonator (DBAR) in TI, integrated it into several system chips, and commercialized it in 2018. He currently holds a senior member, technical staff (SMTS) title and leads the MEMS Research and Development Team along with several university research collaborations in the Kilby Labs, focusing on RF MEMS, nano-mechanical circuits, sensors, and advanced packages.

Dr. Yen is an active reviewer of top MEMS journals, including IEEE JOURNAL OF MICROELECTROMECHANICAL SYSTEMS, and *Sensors*. He is elected as the Vice-Chair of the IEEE San Francisco Bay Area (SFBA) MEMS and Sensor Chapter from 2016 to 2017.

J. Sebastián Gómez-Díaz (Senior Member, IEEE) received the M.S. and Ph.D. degrees in electrical engineering from the Technical University of Cartagena, Cartagena, Spain, in 2006 and 2011, respectively.

He is a Professor with the Electrical and Computer Engineering Department, University of California at Davis, Davis, CA, USA. During the development of his Ph.D., he held visiting research positions with the École Polytechnique de Montréal, Montreal, QC, Canada, and the Fraunhofer Institute for High Frequency Physics and Radar Techniques, Wachtberg, Germany. From 2011 to 2014, he was a Postdoctoral Fellow with the École Polytechnique Fédérale de Lausanne (EPFL), Lausanne, Switzerland. From 2014 to 2016, he continued his postdoctoral work with the Metamaterials and Plasmonic Research Laboratory, The University of Texas at Austin, Austin, TX, USA. His main research interests include applied electromagnetics, plasmonics, 2-D materials, metasurfaces, nonreciprocal and hyperbolic responses, MEMS, and other emerging topics in nanotechnology. As a PI, his research work has been funded by the National Science Foundation, the National Institutes of Health, the U.S. Department of Defense, the Semiconductor Research Corporation, and the Keck Foundation, among other funding agencies.

Dr. Gomez-Diaz is a UC Davis Chancellor Fellow (class of 2023). He received the 2023 UC Davis Graduate Program Advising and Mentoring Award, the 2018 NSF CAREER Award, the 2017 Leopold Felsen Award for Excellence in Electrodynamics, the Raj Mittra Award presented by the 2015 IEEE Antennas and Propagation Society, the Young Scientist Award of the 2015 URSI Atlantic Radio Science Conference, a FP7 Marie Curie Postdoctoral Fellowship from the European Commission in 2012, and the Colegio Oficial de Ingenieros de Telecomunicación (COIT/AEIT) award to the best Spanish Ph.D. thesis in information and communication technologies. He serves as a reviewer for many journals in the fields of engineering and physics.